Optik - International Journal for Light and Electron Optics 265 (2022) 169471

Contents lists available at ScienceDirect

Optik

journal homepage: www.elsevier.com/locate/ijleo

$HE_{1,1}$ mode-excited surface plasmon resonance for refractive index sensing by photonic crystal fibers with high sensitivity and long detection distance

Chao Liu [a,*], Haihao Fu [a], Yan Lv [a], Zao Yi [b], Jiliang Lin [a], Jingwei Lv [a], Lin Yang [a], Paul K. Chu [c]

[a] School of Physics and Electronic Engineering, Northeast Petroleum University, Daqing 163318, PR China
[b] Joint Laboratory for Extreme Conditions Matter Properties, Southwest University of Science and Technology, Mianyang 621010, PR China
[c] Department of Physics, Department of Materials Science and Engineering, and Department of Biomedical Engineering, City University of Hong Kong, Tat Chee Avenue, Kowloon, Hong Kong, PR China

ARTICLE INFO

Keywords:
Optical fiber sensing
Surface plasmon resonance
Photonic crystal fiber
Detection distance

ABSTRACT

Objective: As a result of the rapid development of optical fiber sensing technology, photonic crystal fiber (PCF) sensors based on surface plasmon resonance (SPR) have attracted extensive attention. To design SPR sensor with better performance, a novel ring-core PCF sensor excited by the $HE_{1,1}$ mode is proposed and demonstrated.
Methods: By means of finite element method (FEM) simulation, the structure is optimized and the properties are analyzed systematically with the multi physical field analysis software COMSOL.
Results: The sensor can detect analytes with refractive indexes in the range between 1.34 and 1.425 with average sensitivity and resolution of 13,541.18 nm/RIU and 7.38×10^{-6} RIU respectively, the longest detection distance is 556.59 m. In addition, PCF-SPR sensor has large tolerance in actual manufacturing with the low sensitivity of structural parameters and the amplitude sensitivity of all analytes is above 80 RIU^{-1}. This high-performance sensor has large application potential in biological sensing and oil logging.

1. Introduction

Optical fiber sensing utilizes fibers to sense and transmit the measured signals to realize real-time monitoring [1]. The technology consists of two main parts: modulation and demodulation of the optical signal [2]. In recent years, based on surface plasmon resonance (SPR), the optical fiber sensing technology has attracted enormous attention. SPR is surface sensitive and can detect changes in the dielectric constants when molecules adsorb on metal films [3]. When the external conditions such as stress, frequency, phase, and polarization change, the excited free electrons on the metal surface change concurrently and so sensing can be accomplished on regular patterns. SPR fiber sensors which mainly detect changes of the refractive index are commonly used in biological, military, medical, and other applications [4–6]. Different types of optical fibers can be used as the carrier of SPR, for instance, single-mode fibers (SMFs) [7], multi-mode fibers (MMFs) [8], and so on. However, since these optical fibers have a single structure and poor flexibility, the properties

* Correspondence to: Northeast Petroleum University School of Physics and Electronic Engineering, NO.199, Development Road HIgh Technology dI, Daqing 163318 China.
E-mail address: msm-liu@126.com (C. Liu).

https://doi.org/10.1016/j.ijleo.2022.169471
Received 12 April 2022; Received in revised form 29 May 2022; Accepted 7 June 2022
Available online 9 June 2022
0030-4026/© 2022 Elsevier GmbH. All rights reserved.

are difficult to optimize.

The photonic crystal fiber (PCF) [9–13] is quite flexible in terms of the shape, size, position, and number of air holes in the cladding and more importantly, it has superior bending resistance and excellent nonlinear characteristics thereby boding well for SPR sensing. Therefore, different types of PCF-SPR sensors have been proposed [14–17]. However, most of them excite SPR by the Gaussian fundamental mode, that is, the linear polarization mode $LP_{0,1}$ [18–21], and there has been relatively little research on using mixed modes to excite SPR in optical fibers. Liu et al. [22] have proposed a photonic quasi-crystal fiber (PQF) sensor using the $OAM_{1,1}$ mode to excite SPR for the refractive index range of 1.36–1.435. Unfortunately, the sensitivity of the OAM-SPR sensor is only 4466.5 nm/RIU. The LP mode is formed by superposition of two mixed modes (HE and EH) in the optical fiber. As the fundamental mode of the hybrid mode, the longitudinal component of the $HE_{1,1}$ mode is much smaller than the transverse mode. If SPR is excited by the $HE_{1,1}$ mode, not only can the signal capacity be improved, but also the stability and sensitivity of the fundamental mode can be enhanced.

Herein, a high-sensitivity refractive index sensor with a gold coating on the inner wall on the pores in the cladding is designed for $HE_{1,1}$-excited SPR. The structural parameters of the fiber are investigated numerically and optimized by the finite element method (FEM) analysis using the software COMSOL. The results show that the PCF-SPR sensor can detect analytes in the large refractive index range from 1.34 to 1.425 with excellent sensitivity, detection distance, and resolution of 24 400 nm / RIU, 556.59 m, and 4.098×10^{-6} RIU, respectively. The innovative design and outstanding results provide insights into the design of future PCF-SPR sensors and also reveal the large potential of the device in high-performance refractive index sensing.

2. Basic theory and fiber structure

SPR is a physical-optical phenomenon in which free electrons on the metal-dielectrics interface oscillate under the influence of *p*-polarized light [23]. When the incident light enters the light sparse medium from the light dense medium, it is not reflected directly from the critical interface of the two media, while it transmits through the light sparse medium with a distance of approximate half a wavelength along the interface, and then returns to the light dense medium. The wave traveling along the critical interface is defined as the evanescent wave. In addition, surface plasmon wave (SPW) exists in the metal medium. If the evanescent wave meets the SPW and their propagation constants are identical, that is, phase match conditions are satisfied [24], thus the free electrons on the surface of the metal medium will vibrate collectively and SPR phenomenon is excited.

$$k_{HE_{1,1}} = \frac{\omega_0}{c}\sqrt{\varepsilon_d}\sin\theta_{SPW} = k_{SPW} \tag{1}$$

where ω_0 is the plasmon frequency, c is the speed of light in vacuum, ε_d is the dielectric constant of the object to be measured, and θ_{SP} is the resonance angle.

The working principle of SPR sensing by optical fibers is coupling of surface plasmon polariton (SPP) with the optical fiber guided mode [25]. Under certain phase matching conditions, the fundamental mode excites the SPP mode on the metal-dielectrics surface to produce energy exchange between the fundamental mode light field and metal film surface, resulting in a loss peak with the wavelength corresponding to the maximum loss being the resonance wavelength. The loss of the fundamental mode at different wavelengths is calculated by Eq. (2) [26–28]:

$$L = \frac{2\pi}{\lambda}\frac{20}{\ln(10)}10^4\mathrm{Im}(n_{eff}) \Big/ (dB \Big/ cm) \tag{2}$$

where λ is the wavelength and $\mathrm{Im}(n_{\mathrm{eff}})$ is the imaginary part of effective refractive index of fundamental mode.

The sensitivity and resolution are important parameters of PCF-SPR sensors. By using the slope of the sensor output-input curve, the sensitivity can be obtained by the ratio of the output change to the input change in steady-state operation. With the reduction of optical frequency, the fundamental mode loss increases firstly and then decreases. The wavelength corresponding to the loss peak is defined as the resonance wavelength. The positions of the resonance wavelengths in the loss spectra for different analytes are inconsistent. The corresponding wavelength sensitivity can be obtained by measuring the shift of the resonance wavelength. The sensitivity of the PCF-SPR sensor is expressed by Eq. (3) [29]:

$$S_n = \frac{\Delta\lambda_{peak}}{\Delta n_a} \tag{3}$$

where $\triangle n_a$ and $\triangle\lambda_{peak}$ are the variation of the refractive index of the analyte and offset of the corresponding resonance wavelength, respectively. The resolution is calculated by Eq. (4) [30]:

$$R_n = \frac{\Delta n_a \Delta\lambda_{\min}}{\Delta\lambda_{peak}} = \frac{\Delta\lambda_{\min}}{S_n} \tag{4}$$

where S_n is the sensitivity and $\triangle\lambda_{min}$ is the minimum measured value of the optical spectrum analyzer (OSA), which is generally related to the instrument. Under the current conditions, $\triangle\lambda_{min} = 0.1$ nm.

In order to realize high sensitivity detection by the PCF-SPR sensor and stable generation of the $HE_{1,1}$ mode, a circular PCF is designed as depicted in Fig. 1:

The core of the PCF is the analyte channel with a diameter ***D***. Compared with traditional sensors, the larger channel allows easy

filling of the analyte and reduces the manufacturing complexity. The blue area is the PCF cladding made of SiO_2 and the refractive index is derived by Sellmeier Eq. (5) [31,32]:

$$n^2(\lambda) = 1 + \frac{A_1\lambda^2}{\lambda^2 - B_1} + \frac{A_2\lambda^2}{\lambda^2 - B_2} + \frac{A_3\lambda^2}{\lambda^2 - B_3} \tag{5}$$

where $\boldsymbol{A_1} = 0.6\ 961\ 663$, $\boldsymbol{A_2} = 0.4\ 079\ 426$, $\boldsymbol{A_3} = 0.897\ 479$, $\boldsymbol{B_1} = 0.684\ 043$, $\boldsymbol{B_2} = 0.1\ 162\ 414$, and $\boldsymbol{B_3} = 9.896\ 161$. In order to transmit OAM modes with better performance in the annular region of PCF, it is necessary to design the number of layers of cladding pores reasonably. When there are only two layers, photons are easily leak into the cladding, resulting in distortion of the fundamental mode. When there are four layers of air holes in the cladding, the resonance intensity is too low. Therefore, we set three layers of air holes in the cladding. The layer spacing of the air holes of $\boldsymbol{\Lambda} = 0.12$ μm is compatible with actual production. In the annular region distributing the $HE_{1,1}$ mode, the light field is generated between the first layer of the pore and analyte channel. The inner wall of one of the air holes in the second layer of the pores is plated with a gold film to have stronger antioxidant capacity and the thickness $\boldsymbol{t_g}$ ensures the detection efficiency of the sensor. It should be noted that larger spacing between the fundamental mode and the metal medium will diminish the resonance intensity, while shorter spacing will increase the loss and reduce the detection distance. Therefore, the reason for plating the gold film in the second air hole is to avoid the distance between the gold film and the guide mode being too close or too far, which is more conducive to exciting SPR. The dielectric constant of the gold film is obtained by Drude model [33]:

$$\varepsilon_{Au}(\omega) = \varepsilon_\infty - \frac{\omega_p^2}{\omega(\omega + i\omega_\tau)} \tag{6}$$

where $\varepsilon_\infty = 9.75$, $\omega_p = 1.36 \times 10^{16}$ rad/s, and $\omega_\tau = 1.45 \times 10^{14}$ rad/s. The green region shows the perfectly matched layer (PML) which acts as a good absorber to provide the ideal boundary conditions.

To achieve the best sensitivity, $\boldsymbol{D}$, $\boldsymbol{d}$, $\boldsymbol{t_g}$, and the other parameters of the fiber are optimized for an analyte refractive index of 1.34. The initial structural parameters are $\boldsymbol{D} = 3.6$ μm, $\boldsymbol{d} = 0.96$ μm, and $\boldsymbol{t_g} = 35$ nm. When the diameter of the solution channel to be tested is greater than 4.2 μm, the thickness of the annular area is tiny, and the $HE_{1,1}$ mode is prone to distortion, while too small $\boldsymbol{D}$ will increase the difficulty of injecting the analyte to be tested. In addition, when the diameter of the pore in cladding is less than 0.92 μm, PCF is not easy to be prepared. When $\boldsymbol{d}$ is greater than 1 μm, the loss increases, resulting in a shorter detection distance. In addition, the thickness of gold film is also an important physical parameter to determine the sensitivity of PCF-SPR sensor. When $\boldsymbol{t_g}$ abates from 24 nm, the resonance intensity debases. If the thickness of gold film is greater than 45.5 nm, the sensitivity will be greatly reduced. Consequently, the loss spectra of analytes with refractive indexes of 1.34 and 1.35 are derived for 3.2 μm $\leq \boldsymbol{D} \leq$ 4.2 μm, 0.92 μm $\leq \boldsymbol{d} \leq$ 1 μm, and 25 nm $\leq \boldsymbol{t_g} \leq$ 45 nm. The sensitivity of each one is obtained by Eq. (3) and the results are presented in Fig. 2 (*a*)-(*f*).

By setting $\boldsymbol{d}$ and $\boldsymbol{t_g}$ to 0.96 μm and 35 nm respectively, the fundamental mode losses for the two refractive indexes are calculated when the diameter of the analyte channel is 3.2–4.2 μm. Fig. 2(*a*) and 2(*b*) indicate that the diameter of the analyte passage is directly proportional to the resonance intensity and the resonance wavelength moves towards longer wavelength. The sensitivity increases with *D* and resonance begins to weaken when $\boldsymbol{D} > 4.0$ μm. Therefore, $\boldsymbol{D}$ is set to be 4.0 μm. The effects of the pore diameter in the cladding from 0.92 μm to 1.00 μm on the sensitivity for $\boldsymbol{D} = 4.0$ μm and $\boldsymbol{t_g} = 35$ nm are derived. With decreasing $\boldsymbol{d}$, the resonance wavelength red-shifts and the sensitivity is improved. Although resonance is attenuated, the loss decreases to a more appropriate level, which is conducive to a larger detection distance. The reason why $\boldsymbol{d}$ should be 0.92 μm is that the sensitivity is the highest. The gold film thickness is optimized in the range of 25–45 nm for $\boldsymbol{D}$ and $\boldsymbol{d}$ equal to 4.0 μm and 0.92 μm, respectively. Fig. 2(*f*) shows that when $\boldsymbol{t_g} = 25$ nm, the sensitivity is the highest of 12 490 nm/RIU. Based on the optimization results, $\boldsymbol{D} = 4.0$ μm, $\boldsymbol{d} = 0.92$ μm, and $\boldsymbol{t_g} = 25$ nm.

To produce the PCF, quartz is deposited on the inner wall of the substrate tube which can be removed by dissolution and impurities

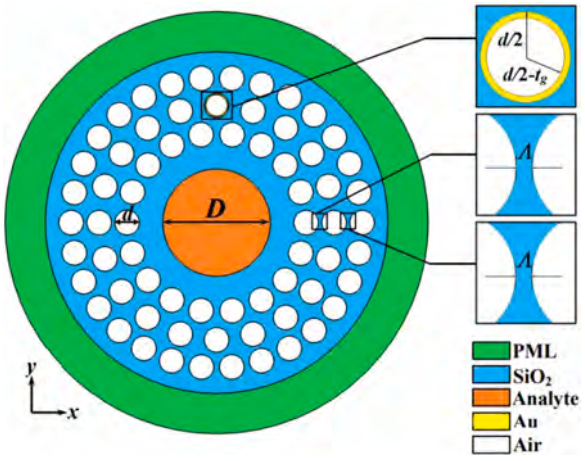

Fig. 1. Cross-section of the circular PCF-SPR sensor.

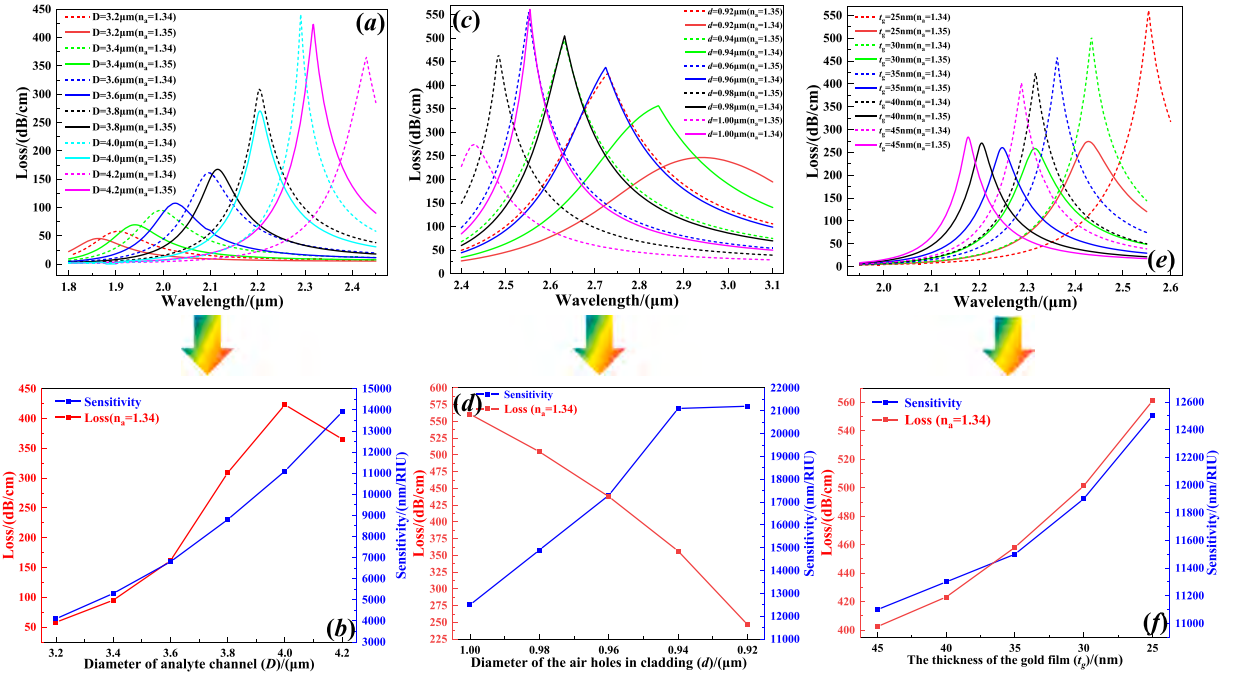

Fig. 2. Loss peaks of $n_a = 1.34$ (dotted line) and 1.35 (solid line) and sensitivity of the PCF-SPR sensor for $n_a = 1.34$: (a)-(b) 3.2 μm ≤ D ≤ 4.2 μm, (c)-(d) 0.92 μm ≤ d ≤ 1 μm, and (e)-(f) 25 nm ≤ t_g ≤ 45 nm.

can be removed by flame polishing. The high-purity quartz tubes are pulled to form capillaries and assembled into bundles to form the PCF preform. Finally, after the preform is pulled into the PCF, the inner wall of the air hole is plated by chemical deposition. The schematic showing refractive index detection by the sensor is exhibited in Fig. 3. SMF is welded to both ends of the PCF injected with the analyte and connected to the light source and OSA, respectively. The loss spectrum of the fundamental mode can be obtained during SPR excitation and the resonance wavelength and resolution can be obtained.

3. Results and discussion

3.1. Coupling properties

The same wave vector correspond to two polarization states (x and y), both of which satisfy the wave equation. Because the light fields of different polarization modes are quite different, it is important to select the appropriate polarization state. As an example, Fig. 4(a) and (b) present the field distributions of the x- and y-polarization modes of the fundamental mode at $\lambda = 2.28$ μm and $n_a = 1.38$. The light field closed to the cladding, and have a pair of red and blue regions is the field distribution in the z direction of $HE_{1,1}$

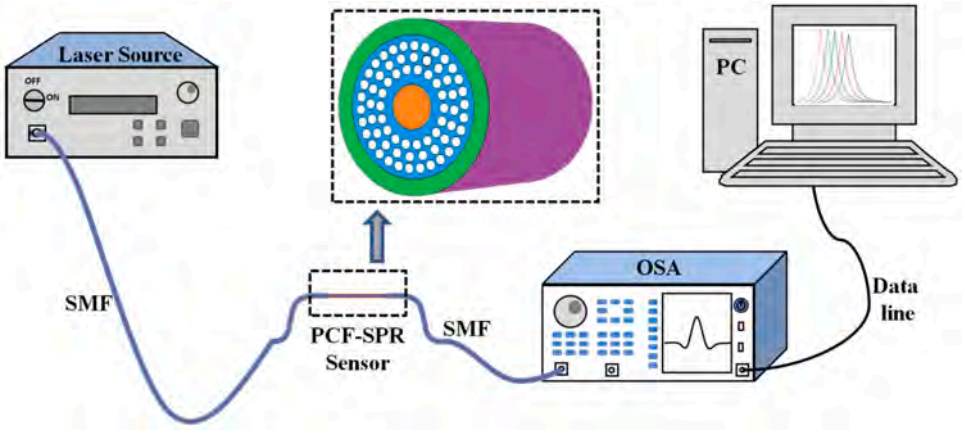

Fig. 3. Schematic of the detection process of the PCF-SPR sensor.

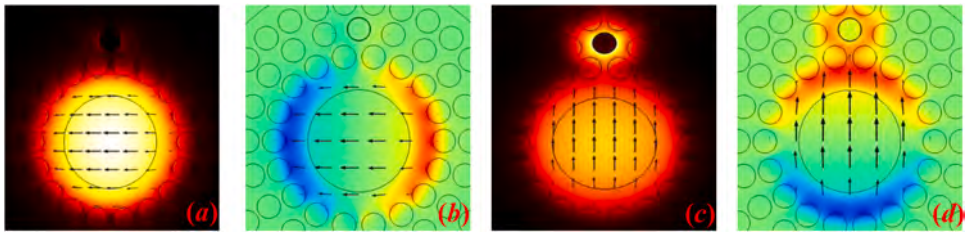

Fig. 4. Field distributions of $HE_{1,1}$ mode: (*a*) *x*-polarization, (*b*) *x*-polarization at *z* direction, (*c*) y-polarization, (*d*) *y*-polarization at *z* direction.

mode.

The black arrow represents the electric field direction in the corresponding mode and the electric field directions of the *x*-polarization mode and *y*-polarization mode are orthogonal to each other. Although both modes have energy coupled to the gold film surface and excite SPR, the resonance intensity of the *y*-polarization mode is significantly higher than that of the *x*-polarization. Consequently, it is more advantageous to use *y*-polarization in the investigation.

After optimizing the parameters of PCF, the $HE_{1,1}$ mode is utilized to excite the SPP mode. Fig. 5(*a*) and (*d*), (*b*) and (*e*), and (*c*) and (*f*) show the fundamental mode and SPP mode at incident wavelengths of 1.8 μm, 2.1 μm, and 2.4 μm ($\boldsymbol{n_a} = 1.40$), respectively. When the wavelength increases, the energy of the basic mode core moves gradually to the surface of the gold film and the energy of the SPP mode increases gradually. When the wavelength is greater than 2.1 μm, the basic mode core energy begins to rise and the energy of the SPP mode decreases. In the vicinity of $\lambda = 2.1$ μm, the energy exchange between the $HE_{1,1}$ mode and SPP mode is the largest and coupling is strongest. Therefore, the resonance wavelength is approximately 2.1 μm when $\boldsymbol{n_a} = 1.40$.

Phase matching between the fundamental mode and SPP mode plays an important role and can be verified by the relationship between the real part of the effective refractive index and wavelength of the $HE_{1,1}$ mode and SPP mode. Fig. 6(*a*) shows the dispersion relationship between the fundamental and SPP mode when the refractive index of the analyte $\boldsymbol{n_a} = 1.40$. With increasing wavelength, the real part of the refractive index of the fundamental mode and SPP mode decreases. When $\lambda = 2.064$ μm, the refractive index of both modes matches and it is called the resonance wavelength at which energy transfer is maximum. The fundamental mode loss also reaches the peak at this wavelength and resonance is strongest as well. Phase matching can also be verified by the variation of the light intensity near the fundamental mode and gold film with wavelength. Fig. 6(*b*) indicates that the light intensity of the $HE_{1,1}$ mode is proportional to the wavelength initially and then inversely proportional to the wavelength to form a wave crest. The light intensity near the gold film is opposite to the $HE_{1,1}$ mode forming a trough. The peak and trough correspond exactly to the same wavelength of $\lambda = 2.064$ μm, i.e. the resonance wavelength.

3.2. *Refractive index sensing*

The refractive index of the analyte is one of the important physical quantities affecting the resonant wavelength and loss peak. Since a wider refractive index detection range is usually preferred in practice, the sensitivity of the sensor should be increased as much as possible. Different analyte refractive indexes give rise to different loss peaks and resonance wavelengths and the degree of coupling between the fundamental mode and SPP mode is also distinct. As shown in Fig. 7(a) and 7(b), the loss spectra of the fundamental mode are calculated for refractive indexes of 1.340–1.365 and 1.370–1.430, respectively, by the parameter scanning method in COMSOL. Fig. 7(*c*) and (*d*) show the resonance wavelength, maximum loss, and sensitivity for $\boldsymbol{n_a} = 1.340$–1.425 to assess the performance of the PCF-SPR sensor.

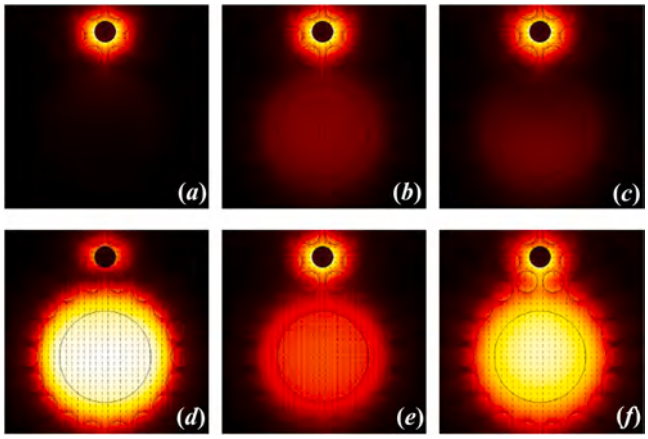

Fig. 5. (*a*)-(*c*) Electric field distributions of the SPP modes and (*d*)-(*f*) $HE_{1,1}$ modes at wavelengths of 1.8 μm, 2.1 μm, and 2.4 μm.

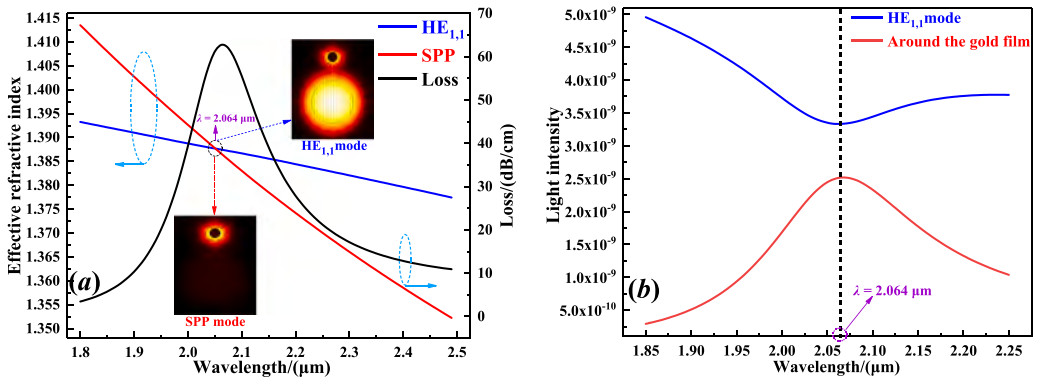

Fig. 6. (a) Relationship between the effective refractive indexes of the fundamental mode, SPP mode, and wavelength; Effects of the wavelength on loss of the fundamental mode: (b) Variation of the light intensity and wavelength near the $HE_{1,1}$ mode and gold film.

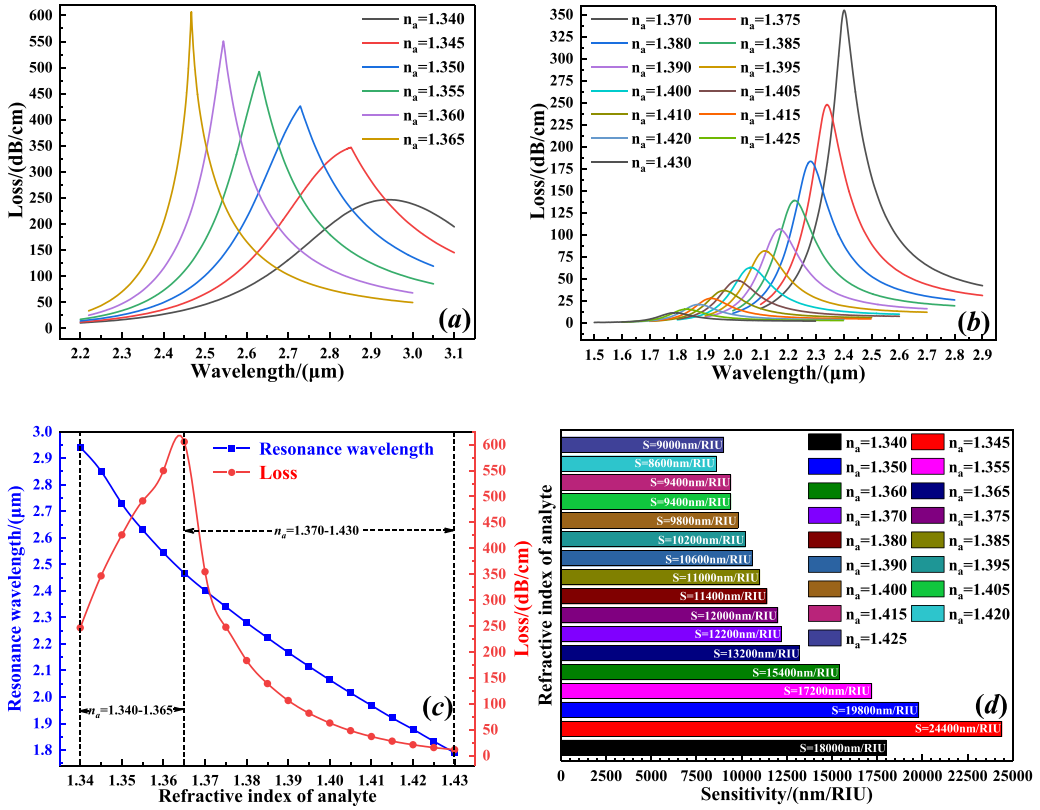

Fig. 7. Loss spectra of the fundamental mode for (*a*) $\boldsymbol{n_a}$ = 1.340–1.365 and (*b*) $\boldsymbol{n_a}$ = 1.370–1.430; (*c*) Resonance wavelength and corresponding maximum loss and (*d*) Sensitivity for $\boldsymbol{n_a}$ = 1.340–1.425.

When the analyte refractive index is 1.365–1.430, the loss of the fundamental mode and resonance intensity increase with increasing wavelength. When $\boldsymbol{n_a}$ = 1.340–1.365, the fundamental mode loss is inversely proportional to the wavelength. Although the energy conversion is reduced, it is still substantial, but a smaller loss is beneficial to increasing the detection distance. When the refractive index goes up, the resonance peak shifts towards short wavelength and the resonance wavelength blue-shifts, indicating stable sensing by coupling the $HE_{1,1}$ and SPP modes. The refractive index and resonance wavelength of the adjacent loss peaks are employed to derive the sensitivity as shown in Fig. 7(d). With increasing $\boldsymbol{n_a}$, the sensitivity of the PCF-SPR sensor drops but still is greater than 8600 nm/RIU. The maximum sensitivity is 24 400 nm/RIU ($\boldsymbol{n_a}$ = 1.345) and the average sensitivity is 13,541.18 nm/RIU. By acquiring the curve and approximate expression of the resonance wavelength with respect to the refractive index of the analyte a shown in Eq. (7) and Fig. 8(a), respectively, numerical fitting can be implemented:

$$\lambda_R = 19.29 - 12.27 n_a \tag{7}$$

where $\boldsymbol{\lambda_R}$ is the resonance wavelength and $\boldsymbol{n_a}$ is the refractive index of the analyte which is between 1.340 and 1.430. The R-square value is 97.58 %. The resolution for different $\boldsymbol{n_a}$ can be obtained by Eq. (4). The best resolution is 4.10×10^{-6} RIU and the average resolution is 7.38×10^{-6} RIU.

3.3. Structural parameter sensitivity

The structural parameters of the PCF are very sensitive to the transmission characteristics of the fundamental mode and even a minute change can impact the sensing performance. In practice, the actual properties frequently deviate from theoretical simulation due to the small parameter deviation in the production process. Therefore, the impact of structural parameters on the sensor characteristics should be reduced as much as possible when designing the PCF-SPR sensor in order to achieve stable detection. The ratio of the offset to the parameter change can be used to gauge the sensitivity of the structural parameters to sensor performance, which is termed the parameter sensitivity. Fig. 9(*a*)−(*c*), (*d*)−(*f*), and (*g*)−(*i*) describe the parameter sensitivity of the analyte channel diameter, cladding pore diameter, and gold film thickness for an refractive index of $\boldsymbol{n_a} = 1.34$.

With regard to the analyte channel as shown in Fig. 9(*a*)−(*c*), when $\boldsymbol{D}$ is increased, the loss peak shifts to longer wavelength and the resonance wavelength red-shifts. The distance between the fundamental mode and gold film decreases when the analyte channel expands, and energy coupling between $HE_{1,1}$ and SPP mode increases like the parameter sensitivity. As for the cladding pore diameter, Fig. 9(*d*)−(*f*) show that when the cladding pore diameter increases, the change of the loss peak and resonance wavelength is consistent with that of the analyte channel. The reason why the resonance intensity decreases is that the spacing between the cladding pores decreases consequently hinder energy exchange between the basic mode and SPP mode. At the same time, the overall parameter sensitivity shows a downward trend, which is beneficial to refractive index detection. Fig. 9(*g*)−(*i*) show that the gold film thickness is inversely proportional to the resonance wavelength and fundamental mode loss and hence, the film thickness has a great influence on the parameter sensitivity as manifested by the downward trend overall. The minimum parameter sensitivities of $\boldsymbol{D}$, $\boldsymbol{d}$, and $\boldsymbol{t_g}$ are 450 nm/μm, 3300 nm/μm and 0.346 μm/nm and the average parameter sensitivities are 516 nm/μm, 4655.4 nm/μm, and 0.0532 μm/nm, respectively, which are very small compared to the wavelength sensitivity boding well for high-performance refractive index detection.

3.4. Amplitude sensitivity

Wavelength interrogation is widely utilized to detect the sensitivity of PCF-SPR sensor, but the loss spectra of different analytes are difficult to operate in practice. In order to make the measurement of sensitivity easier, it can be detected by observing the change of optical power transmitted by different analytes at fixed wavelength. It can be calculated by amplitude sensitivity in formula (8) [34]:

$$S_A = -\frac{1}{\alpha(\lambda, n_a)} \frac{\partial \alpha(\lambda, n_a)}{\partial n_a} \tag{8}$$

where $\alpha(\lambda, n_a)$ is the loss of the analyte at a certain wavelength and $\partial\alpha(\lambda, n_a)$ and ∂n_a are the differences of the loss and refractive index of adjacent analytes, respectively. Fig. 10 shows the variation of amplitude sensitivity corresponding to different analytes.

It is seen from Fig. 10 that the amplitude sensitivity firstly decreases and then increases with the red shift of wavelength. It should be noted that maximum amplitude sensitivities change unobviously for the refractive index of 1.340–1.425. For $1.340 \leq \boldsymbol{n_a} \leq 1.360$, the maximum amplitude sensitivities increase with increasing the refractive index of the analyte. The maximum amplitude sensitivities are negative for the refractive index of $1.365 \leq \boldsymbol{n_a} \leq 1.425$. In addition, the amplitude sensitivity of all analytes is above 80 RIU^{-1}, and the maximum amplitude sensitivity is 278.45 RIU^{-1} ($\boldsymbol{n_a} = 1.360$).

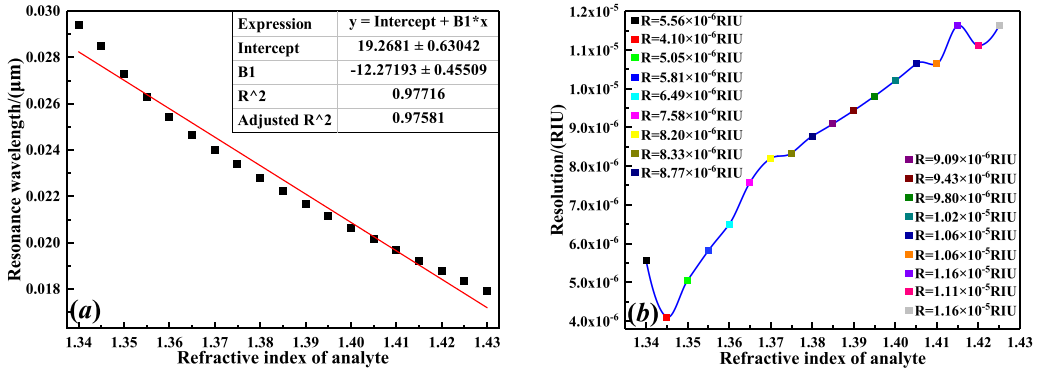

Fig. 8. (*a*) Numerical fitting of the resonance wavelength with respect to the analye refractive index and (*b*) Resolution of the PCF-SPR sensor.

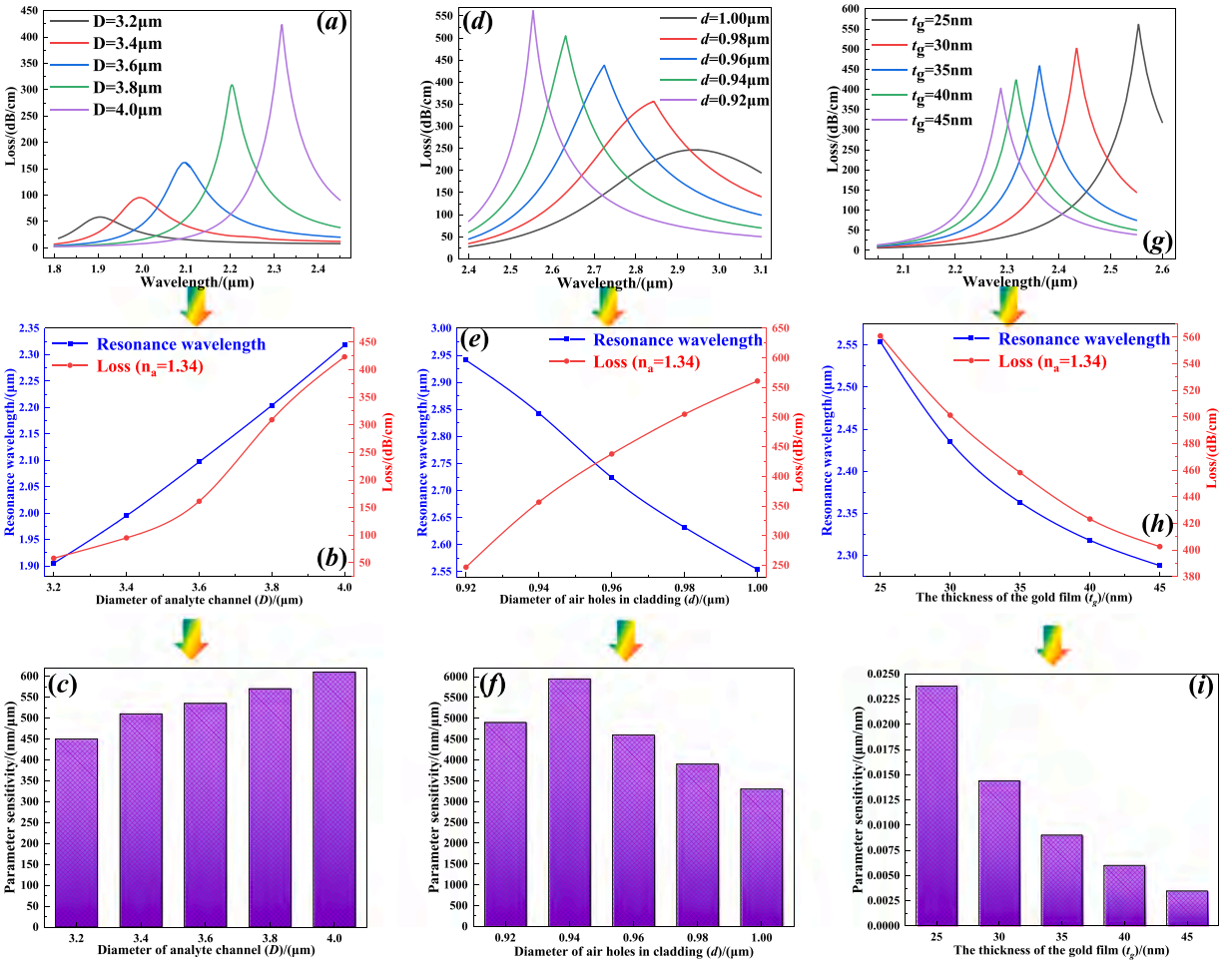

Fig. 9. Parameter variation, resonance wavelength and loss, and parameter sensitivity: (*a*)-(*c*) analyte channel diameter, (*d*)-(*f*) Cladding pore diameter, and (*g*)-(*i*) Gold film thickness for n_a = 1.34.

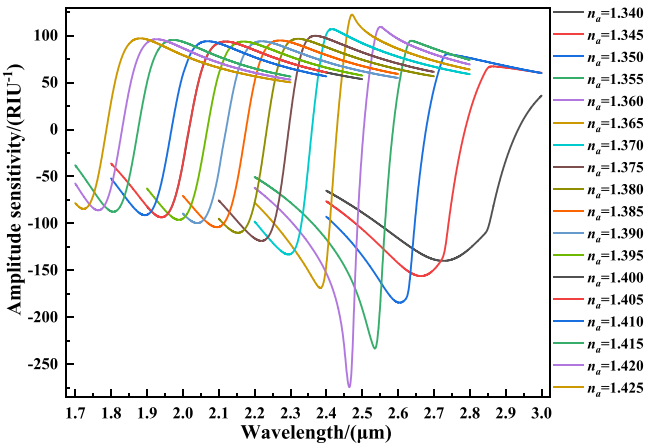

Fig. 10. Amplitude sensitivity of different analytes.

3.5. Detection distance

In practice, PCF-SPR sensors are often deployed in complex environments. If the signal transmission distance of the PCF is too short, there will be problems associated with the reduced conversion efficiency of optical and electrical signals, signal distortion, and compromised detection accuracy. The fundamental mode of SPR sensing is composed of the odd mode and even mode. The transmission rates of the odd and even modes are different in optical fibers consequently resulting in the walk-off effect. If the distance between the fast and slow modes is too large, high walk-off effects result and the fundamental mode can no longer be composed. The 10 *ps* walk-off length expressed in Eq. (9) [35] is a physical quantity used to compute the maximum distance of the fundamental mode propagating in the structure to measure the detection distance of PCF-SPR sensor:

$$L_{10ps} = \frac{c \times 10ps}{n_{eff}^{even} - n_{eff}^{odd}} = \frac{3 \times 10^{-3}}{n_{eff}^{even} - n_{eff}^{odd}}(m) \tag{9}$$

where c is the speed of light, and $n_{even\ eff}$and $n_{odd\ eff}$are the effective refractive indexes of the even and odd mode, respectively. Fig. 10(*a*) and (*b*) display the 10 *ps* walk-off length when the refractive indexes of the analyte are 1.34, 1.38 and 1.42, respectively, as well as the 10 *ps* walk-off length of the fundamental mode of the PCF-SPR sensor for different $\boldsymbol{n_a}$.

As shown in Fig. 11(a), taking $\boldsymbol{n_a} = 1.34$, 1.38, and 1.42 as examples, the variation of the 10 *ps* walk-off length with wavelength is determined. The 10 *ps* walk-off length decreases when the wavelength increases. Fig. 11(b) shows the 10 *ps* walk-off lengths of different analytes at the resonance wavelengths and the walk-off length decreases gradually when the resonance wavelength red-shifts. When $\boldsymbol{n_a} \geq 1.370$, the detection distance increase significantly, as shown by a minimum of 39.8853 m and maximum of 556.8563 m, which benefit long-distance detection. The walk-off length of an analyte with a large refractive index is greater than that of an analytes with a small refractive index. Consequently, the PCF-SPR sensor is more suitable for detecting analytes with larger refractive indexes.

3.6. FOM and SNR

As a physical quantity to gauge the overall performance of the PCF-SPR sensor, the figure of merit (FOM) can be derived by Eq. (10) [36]:

$$FOM = \frac{S_n}{FWHM} \tag{10}$$

where S_n is the sensitivity for each analyte refractive index and FWHM is the full-width at half-maximum. Fig. 12(*a*) describes the relationship between FOM and analyte refractive indexes. The FOM increases first and then decreases with red-shifting of $\boldsymbol{n_a}$ and shows the maximum of 153.214 RIU^{-1} when the refractive index is 1.365. The signal-to-noise ratio (SNR) determined by Eq. (11) [36] is another entity affecting the sensing characteristics:

$$SNR = \frac{\Delta\lambda_R}{FWHM} \tag{11}$$

where $\triangle\lambda_R$ is the difference between two adjacent resonant wavelengths. Fig. 12(*b*) presents the SNR for $\boldsymbol{n_a}$ between 1.34 and 1.425 and the variation trend with refractive indexes is basically consistent with that of the FOM. When $\boldsymbol{n_a} = 1.365$, the maximum SNR is 0.7661.

3.7. Performance comparison

In order to illustrate the advantages of the PCF-SPR sensor, the properties are compared to those of similar sensors reported in the

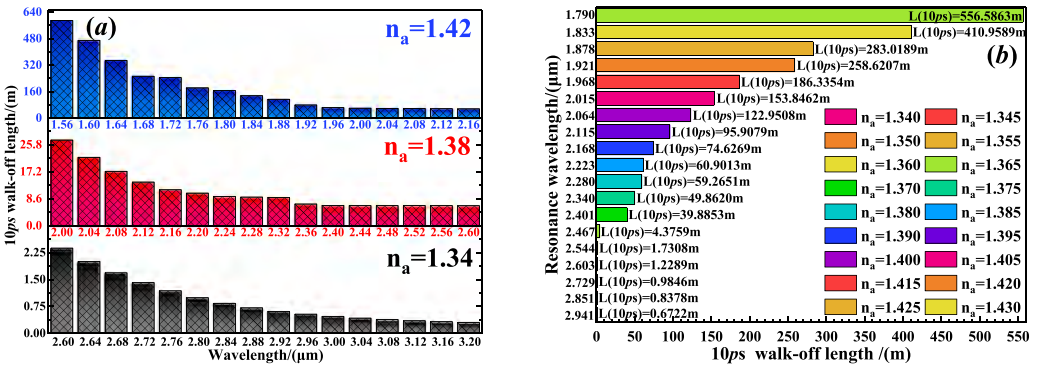

Fig. 11. (*a*) 10 *ps* walk-off length for refractive indexes of 1.34, 1.38, and 1.42 and (*b*) 10 *ps* walk-off length of the fundamental mode of the PCF-SPR sensor for different $\boldsymbol{n_a}$.

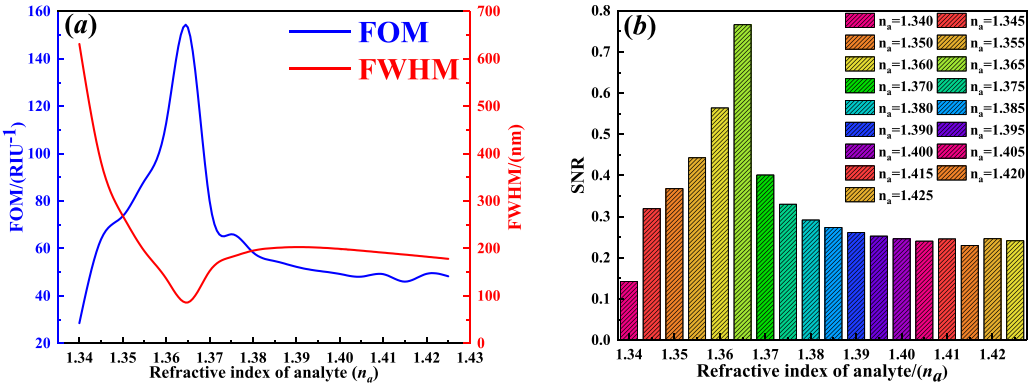

Fig. 12. Relationship between (*a*) FOM and (*b*) SNR and refractive indexes of analytes.

Table 1
Performance comparison with other PCF-SPR sensors.

Ref	Fiber structure	Film	Mode excited SPR	The range of n_a	Wave sensitivity	Wave resolution
Ref.[36]	D-shaped PCF	Au	$LP_{0,1}$ mode	1.330–1.400	14 933.3 nm/RIU	6.69×10^{-6} RIU
Ref.[37]	H-shaped PCF	Ag	$LP_{0,1}$ mode	1.330–1.410	12 600 nm/RIU	3.61×10^{-5} RIU
Ref.[38]	Air-core PCF	Au	$LP_{0,1}$ mode	1.330–1.410	11 700 nm/RIU	8.55×10^{-6} RIU
Ref.[39]	Horizontal polishing PCF	Au	$LP_{0,1}$ mode	1.330–1.400	11 600 nm/RIU	8.62×10^{-6} RIU
Ref.[40]	Circular double core PCF	Au	$LP_{0,1}$ mode	1.330–1.440	11 200 nm/RIU	8.92×10^{-6} RIU
Ref.[41]	Hollow core C-shaped PCF	Ag	$LP_{0,1}$ mode	1.330–1.420	21 000 nm/RIU	4.76×10^{-6} RIU
Ref.[42]	D-shaped PCF	Au	$LP_{0,1}$ mode	1.420–1.460	15 000 nm/RIU	–
Ref.[43]	Ring-core PQF	Ag	$OAM_{1,1}$ mode	1.360–1.435	4466.5 nm/RIU	2.30×10^{-5} RIU
This paper	*Ring-core PCF*	*Au*	*$HE_{1,1}$ mode*	*1.340–1.430*	*24 400 nm/RIU*	*4.098×10^{-6} RIU*

recent literature. Table 1 shows the comparison of the structure, mode exciting SPR, refractive index detection range, wavelength sensitivity, and resolution.

Compared to the PCF described in this paper, the arrangement of the cladding pores in most other PCF-SPR structures have no obvious regularity and they are difficult to manufacture. In addition, most fibers use the $LP_{0,1}$ mode to excite SPR, whereas the $HE_{1,1}$ mode is utilized in the sensor described here for easier excitation and broader refractive index detection range. As a result, the sensor exhibits a high sensitivity of 24,400 nm/RIU as well as resolution of 4.098×10^{-6} RIU, which are better those of most other sensors.

4. Conclusion

A PCF refractive index sensor based on $HE_{1,1}$ mode-excited SPR is designed and analyzed. The COMSOL software is adopted to optimize the diameter of the analyte channel, cladding pore diameter, and film thickness. Numerical analysis indicates that the fundamental mode and SPP mode have good phase matching and stable detection of analyte refractive indexes in the range of 1.34–1.43 is demonstrated. When the refractive index of the analyte is 1.345, the wavelength sensitivity is the largest (24 400 nm/RIU) and the resolution is the highest as well. The longest detection distance of the PCF-SPR sensor is 556.85 m that is sufficient for most applications. The sensor with excellent properties have enormous potential in biological analysis, chemical detection, and related applications.

Declaration of Competing Interest

The authors declare no conflicts of interest.

Acknowledgments

This work was jointly supported by Local Universities Reformation and Development Personnel Training Supporting Project from Central Authorities [140 119 001], City University of Hong Kong Strategic Research Grant (SRG) [7 005 505], and Scientific Research Fund of Sichuan Province Science and Technology Department [2020YJ0137].

References

[1] H. Thenmozhi, M.S. Mani Rajan, K. Ahmed, P.C.F. D-shaped, Sensor based on SPR for the detection of carcinogenic agents in food and cosmetics, Optik 180 (2019) 264–270.

[2] Z. Lin, J.Y. Yang, M. Song, et al., Microring-based modulation and demodulation of DPSK signal, Opt. Express 15 (2007) 11564–11569.
[3] J. Homola, S.S. Yee, G.N. Gauglitz, Surface plasmon resonance sensors: review, Sens. Actuators B: Chem. 54 (1999) 3–15.
[4] A. Ha, B. Kaa, A. Sam, Ultrahigh sensitivity refractive index biosensor based on gold coated nano-film photonic crystal fiber, Results Phys. 17 (2020), 103151. ScienceDirect.
[5] Y. Liu, H. Chen, Y. Guo, et al., Ultra-high sensitivity plasmonic sensor based on D-shaped photonic crystal fiber with offset-core, Opt. - Int. J. Light Electron Opt. 221 (2020), 165309.
[6] S. Shingh, Y.K. Prajapati, TiO2/gold-graphene hybrid solid core SPR based PCF RI sensor for sensitivity enhancement, Opt. - Int. J. Light Electron Opt. 224 (2020), 165525.
[7] G.J. Tearney, S.A. Boppart, B.E. Bouma, et al., Scanning single-mode fiber optic catheter–endoscope for optical coherence tomography, Opt. Lett. 21 (1996) 543–545.
[8] P. Pepeljugoski, S.E. Golowich, A.J. Ritger, et al., Modeling and simulation of next-generation multimode fiber links, Light. Technol. J. 21 (2003) 1242–1255.
[9] E. Liu, S. Liang, J. Liu, Double-cladding structure dependence of guiding characteristics in six-fold symmetric photonic quasi-crystal fiber, Superlattices Microstruct. 130 (2019) 61–67.
[10] E. Liu, W. Tan, B. Yan, J. Xie, R. Ge, J. Liu, Robust transmission of orbital angular momentum mode based on a dual-cladding photonic quasi-crystal fiber, J. Phys. D: Appl. Phys. 52 (2019), 325110.
[11] C. Li, B. Yan, J. Liu, Refractive index sensing characteristics in a D-shaped photonic quasi-crystal fiber sensor based on surface plasmon resonance, J. Opt. Soc. Am. A 36 (2019) 1663–1668.
[12] E. Liu, W. Tan, B. Yan, J. Xie, R. Ge, J. Liu, Broadband ultra-flattened dispersion, ultra-low confinement loss and large effective mode area in an octagonal photonic quasi-crystal fiber, J. Opt. Soc. Am. A 35 (2018) 431–436.
[13] B. Yan, A. Wang, E. Liu, W. Tan, J. Xie, R. Ge, J. Liu, Polarization filtering in the visible wavelength range using surface plasmon resonance and a sunflower-type photonic quasi-crystal fiber, J. Phys. D: Appl. Phys. 51 (2018), 155105.
[14] A.A. Revathi, D. Rajeswari, Surface plasmon resonance biosensor-based dual-core photonic crystal fiber: design and analysis, J. Opt. 49 (2020) 163–167.
[15] G. An, S. Li, X. Yan, et al., Extra-broad photonic crystal fiber refractive index sensor based on surface plasmon resonance, Plasmonics 12 (2017) 465–471.
[16] X. Guo, L. Han, F. Liu, et al., Refractive index sensing characteristics of dual-core PCF based on surface plasmon resonance, Opt. - Int. J. Light Electron Opt. 218 (2020), 164796.
[17] N. Luan, W. Ran, W. Lv, et al., Surface plasmon resonance temperature sensor based on photonic crystal fibers randomly filled with silver nanowires, Sensors 14 (2014) 16035–16045.
[18] Q.L. Wu, Y. Zhao, Y.N. Zhang, et al., Characteristics of a new multi-channel sensing device based on C-type photonic crystal fibers, Opt. Laser Technol. 134 (2021), 106622.
[19] Y.E. Monfared, M. Qasymeh, Plasmonic biosensor for low-index liquid analyte detection using graphene-assisted photonic crystal fiber, Plasmonics 16 (2021) 881–889.
[20] J. Lou, T. Cheng, S. Li, et al., Surface plasmon resonance photonic crystal fiber biosensor based on gold-graphene layers, Opt. Fiber Technol. 50 (2019) 206–211.
[21] M.R. Hasan, S. Akter, A.A. Rifat, et al., Spiral photonic crystal fiber-based dual-polarized surface plasmon resonance biosensor, IEEE Sens. J. 18 (2017) 133–140.
[22] E. Liu, B. Yan, H. Zhou, et al., OAM mode-excited surface plasmon resonance for refractive index sensing based on photonic quasi-crystal fiber, J. Opt. Soc. Am. B 38 (2021) F16–F22.
[23] Liu Chao, L.ü Jingwei, Liu Wei, Wang Famei, K.Chu Paul, Overview of refractive index sensors comprising photonic crystal fibers based on the surface plasmon resonance effect [Invited], Chin. Opt. Lett. 19 (2021), 102202.
[24] P.S. Tan, X.C. Yuan, J. Lin, et al., Surface plasmon polaritons generated by optical vortex beams, Appl. Phys. Lett. 92 (2008) 171.
[25] M.S. Aruna Gandhi, K. Senthilnathan, P. Ramesh Babu, et al., Highly sensitive localized surface plasmon polariton based D-type twin-hole photonic crystal fiber microbiosensor: enhanced scheme for SERS reinforcement, Sensors 20 (2020) 5248.
[26] H. Fu, Z. Yi, Y. Shi, et al., Circular anti-resonance fibre supporting orbital angular momentum modes with flat dispersion, high purity and low confinement loss, J. Mod. Opt. 68 (2021) 784–791.
[27] H. Fu, C. Liu, C. Hu, et al., Circular photonic crystal fiber supporting 118 orbital angular momentum modes transmission, Opt. Eng. 60 (2021), 076102.
[28] H. Fu, M. Zhu, C. Liu, et al., Photonic crystal fiber supporting 394 orbital angular momentum modes with flat dispersion, low nonlinear coefficient, and high mode quality, Opt. Eng. 61 (2022), 026111.
[29] D. Gao, C. Guan, Y. Wen, et al., Multi-hole fiber based surface plasmon resonance sensor operated at near-infrared wavelengths, Opt. Commun. 313 (2014) 94–98.
[30] M. Gandhi, S. Sivabalan, P.R. Babu, et al., Designing a biosensor using a photonic quasi-crystal fiber, IEEE Sens. J. 16 (2016) 2425–2430.
[31] Liu Wei, Shi Ying, Yi Zao, Liu Chao, Wang Famei, Li Xianli, Lv Jingwei, Yang Lin, K.Chu Paul, Surface plasmon resonance chemical sensor composed of a microstructured optical fiber for the detection of an ultra-wide refractive index range and gas-liquid pollutants, Opt. Express 29 (2021) 40734–40747.
[32] H. Fu, Y. Shi, Z. Yi, et al., Effects of air holes in the cladding of photonic crystal fibers on dispersion and confinement loss of orbital angular momentum modes, Opt. Quantum Electron. 54 (2022) 1–17.
[33] H.S. Sehmi, W. Langbein, E.A. Muljarov, Optimizing the Drude-Lorentz model for material permittivity: Method, program, and examples for gold, silver, and copper, Phys. Rev. b. 95 (2017), 115444.
[34] Chao Liu, Haihao Fu, Chunjie Hu, Lei Zhou, Ying Shi, Jingwei Lv, Lin Yang, Paul K. Chu, Optimization of photonic crystal fibers for transmission of orbital angular momentum modes, Opt. Quantum Electron. 53 (2021) 1–18.
[35] F. Zha, J. Li, P. Sun, et al., Highly sensitive selectively coated D-shape photonic crystal fibers for surface plasmon resonance sensing, Phys. Lett. A 383 (2019) 1825–1830.
[36] Firoz, Haider, Rifat, et al., Highly amplitude-sensitive photonic-crystal-fiber-based plasmonic sensor, JOSA B. 35 (2018) 2816–2821.
[37] S. Singh, Y.K. Prajapati, Dual-polarized ultrahigh sensitive gold/MoS_2/graphene based D-shaped PCF refractive index sensor in visible to near-IR region, Opt. Quantum Electron. 52 (2020) 1–15.
[38] Zhu Li, Yang, et al., A refractive index sensor based on H-shaped photonic crystal fibers coated with ag-graphene layers, Sensors 20 (2020) 741.
[39] A.K. Paul, M.S. Habib, N.H. Hai, et al., An air-core photonic crystal fiber based plasmonic sensor for high refractive index sensing, Opt. Commun. 464 (2020), 125556.
[40] P. Bing, J. Sui, G. Wu, et al., Analysis of dual-channel simultaneous detection of photonic crystal fiber sensors, Plasmonics 15 (2020) 1071–1076.
[41] Q.M. Kamrunnahar, J.R. Mou, M. Momtaj, Dual-core gold coated photonic crystal fiber plasmonic sensor: design and analysis, Results Phys. 18 (2020), 103319.
[42] M.B. Hossain, S. Islam, K. Hossain, et al., High sensetivity hollow core circular shaped pcf surface plasmonic biosensor employing silver coat: a numerical design and analysis with external sensing approach, Results Phys. 16 (2020), 102909.
[43] M.B. Hossain, T.V. Mahendiran, L.F. Abdulrazak, et al., Numerical analysis of gold coating based quasi D-shape dual core PCF SPR sensor, Opt. Quantum Electron. 52 (2020) 1–13.